Modeling of a light-fueled self-paddling boat with a liquid crystal elastomer-based motor

Haiyang Wu, Chongfeng Zhao, Yuntong Dai, and Kai Li*
School of Civil Engineering, Anhui Jianzhu University, Hefei, Anhui 230601, China

(Received 27 August 2023; accepted 12 March 2024; published 29 April 2024)

Active materials possess unique properties of being able to respond autonomously to external stimuli, yet realizing and regulating the motion behavior of active machines remains a major challenge. Conventional control approaches, including sensor control and external device control, are both complex and difficult to implement. In contrast, active materials–based self-oscillators offer distinct properties such as periodic motion and ease of regulation. Inspired by paddle boats, we have proposed a conceptual light-fueled self-paddling boat with a photothermally responsive liquid crystal elastomer (LCE)–based motor that operates under steady illumination and incorporates an LCE fiber. Based on the well-established dynamic LCE model and rotation dynamics, the dynamic equations for governing the self-paddling of the LCE-steered boat are derived, and the driving torque of the LCE-based motor and the paddling velocity of the LCE-steered boat are formulated successively. The numerical results show that two motion modes of the boat under steady illumination: the static mode and the self-paddling mode. The self-paddling regime arises from the competition between the light-fueled driving torque and the frictional torque. Moreover, the critical conditions required to trigger the self-paddling are quantitatively examined as well as the significant system parameters affecting the driving torque, angular velocity, and paddling velocity. The proposed conceptual light-fueled self-paddling LCE-steered boat exhibits benefits including customizable size and being untethered and ambient powered, which provides valuable insights into the design and application of micromachines, soft robotics, energy harvesters, and beyond.

DOI: 10.1103/PhysRevE.109.044705

I. INTRODUCTION

Active materials constitute a class of materials with a distinctive nature that enables them to respond autonomously to external stimuli [1]. These materials can convert various forms of energy such as light [2], heat [3], and magnetic [4] and electrical energy [5] into mechanical energy, leading to their own deformation and motion, which finds significant applications in fields of autonomous robotics [6–12] and autonomous controllers. Meanwhile, a diverse range of active materials including hydrogels [13,14], ionogels [15,16], piezoelectric materials [17], shape memory alloys [18], and liquid crystal elastomers (LCEs) [19–21] has gained research attention owing to their characteristics of structural integration, controllable weight, low noise, environmental friendliness, and recoverability. Consequently, they hold great promise in smart structures [6], bionic organs [12], aerospace [22], and beyond.

Conventional control approaches include sensor control and external device control, where sensors are utilized to perceive the states of active machines [23] and their surroundings [24]. Subsequently, feedback control algorithms are employed to adjust the response of active materials in time to achieve precise control. With the rapid development of artificial intelligence, electronic information technology, machine learning, and network technology are expected to further facilitate the intelligent control of active machines [25]. Nevertheless, most of these control approaches require a complex control center, akin to the control of the human body by the brain [26,27]. This complexity and the demand for accuracy present a formidable challenge that impedes the design and application of active machines.

Self-oscillations have great potential and advantages in controlling active machines [25]. Self-oscillating systems are systems that absorb energy from a steady external environment to maintain their own motion [28,29]. Attributed to their distinctive nature, there has been a surge of research interest in active materials–based self-oscillators [30]. Self-oscillating systems can autonomously generate periodic and continuous vibrations without any external excitation or input because of their internal feedback mechanisms and inherent nonlinear properties. Self-oscillations are manifested in various systems, such as the swing of a pendulum, electronic oscillating circuits, and the rhythmic beating of a heart, where the system energy is continuously converted and periodically dissipated to sustain the oscillatory state [31]. Simple structures often enable the realization of these periodic motion modes [32,33], thus facilitating the design of self-oscillating machines. Additionally, self-oscillating systems demonstrate robustness [34], with amplitudes and frequencies being dependent upon system parameters and independent of initial conditions, thereby aiding in the realization and regulation of active machines [35–37]. The numerous benefits of self-oscillators make them an attractive source of inspiration for applications in active machines [6,7], energy harvesting [38,39], engines [40], and autonomous robotics [41].

A great variety of self-oscillating systems [42] has been constructed employing active materials like LCEs, ionic

*kli@ahjzu.edu.cn

gels, and hydrogels. These systems exhibit a range of self-oscillatory modes, including oscillating [43,44], spinning [45], rolling [46], bending [47,48], jumping [49], chaos [50], synchronization [51], and floating [52]. Several feedback mechanisms have been devised to acquire stable energy for self-oscillating systems, including the self-masking mechanism [53], chemical reaction coupled with large deformation [16], liquid volatilization coupled with deformation [54], and the photothermal surface tension gradient mechanism [55]. Among various stimulus-responsive materials [56], LCEs [19–21,57] have garnered substantial attention due to their remarkable features, such as large and reversible deformation, rapid response, and easy control. LCEs can respond to various stimuli such as light [58,59], heat [60–63], and electricity [64,65]. The photothermally responsive LCE exhibits fast response, environmental friendliness, easy accessibility, noiselessness, and precise control [36,43]. These self-oscillating systems hold significant promise in the domains of bionic instrumentation [66,67], energy harvesting [38,39], and autonomous robotics [68,69].

While self-oscillating units based on active materials have demonstrated notable achievements, there is still a need to construct various active machines using these units to unlock additional functions and applications. The origins of this type of motor can be traced back to Steinberg's proposal of the mechanical chemical motor [70]. Similarly, Knežević and Warner introduced a conceptual photomechanical elastomer engine and a mechanical turbine motor [71,72]. However, the realization of these proposed motors has been hindered by the limitations in the response speed of the active material. With the continuous in-depth study of active materials, researchers such as He *et al.* [6] and Xing *et al.* [61] developed an LCE fiber oscillator with an oscillation period down to 0.1 s, which provides potential for realizing the previously envisioned LCE-based motor. Inspired by paddle boats, this paper proposes a light-fueled self-paddling LCE-steered boat which can move forward sustainably under steady illumination using the drive belt structure of an LCE fiber as the motor. In this paper, we aim to propose a conceptual light-fueled self-paddling boat with a photothermally responsive LCE-based motor, describe its dynamic behavior, study its operating conditions, and provide guidance for its practical applications. The proposed self-paddling boat system has the unique advantages of simple structure, customizable size, and being untethered and ambient powered, and it can be miniaturized and integrated, making it easier to be practically applied in micromachines and systems. This paper has the potential to boost practical applications in the fields of autonomous robotics, microsensors, reconnaissance and surveillance, and energy harvesting.

The remainder of this paper is structured as follows. In Sec. II, the nonlinear dynamics model of the self-paddling boat system under steady illumination is introduced. Based on the well-established dynamic LCE model and rotation dynamics, the corresponding governing equations are derived, and the driving torque of the LCE-based motor and the paddling velocity of the LCE-steered boat are formulated successively. In Sec. III, the focus is on the critical conditions for triggering the self-paddling and the influences of different system parameters on self-paddling, including the driving torque of the LCE-based motor, the angular velocity of the wheel, and the paddling velocity of the LCE-steered boat. Finally, in Sec. IV, this paper is summarized, and potential future directions are outlined.

II. THEORETICAL MODEL AND FORMULAS

In this section, we describe a light-fueled self-paddling boat system consisting of a photothermally responsive LCE fiber acting as a motor, four rotating wheels, and several paddles. The governing equations of the self-paddling LCE-steered boat are then derived based on the dynamic LCE model and rotation dynamics. Finally, the governing equations are nondimensionalized by introducing dimensionless system parameters.

A. Dynamics of the self-paddling LCE-steered boat

Inspired by the paddle boat, an LCE-steered boat that can self-paddle under steady illumination is constructed. Figs. 1(a) and 1(b) depict the theoretical model of the self-paddling LCE-steered boat, which consists of a photothermally responsive LCE fiber, four rotating wheels, and several paddles. The LCE fiber employed in this paper is composed of either thiol-acrylate or siloxane LCE, showcasing substantial elastic strains [73]. In the reference state illustrated in Fig. 1(c), the LCE fiber is stress free, possessing an original length of L_0. Meanwhile, the LCE fiber exists in a monodomain state, with liquid-crystal mesogens aligned along the longitudinal direction. Then the LCE fiber is prestretched and placed on two wheels, as shown in Fig. 1(b). The radius of the large wheel 1 (i.e., the master wheel) is R_1, while the radius of the small wheel 2 (i.e., the follower wheel) is R_2. In the initial state, the stretched length of the LCE fiber is L, and its stretch rate is λ_0, which is defined as the ratio of the current length L to the original length L_0.

In the current state, steady illumination is applied onto a portion of the LCE fiber, as shown by the yellow region in Fig. 1(d). When the LCE fiber is exposed to illumination and heated, it contracts along the longitudinal direction due to the transition from the monodomain to the isotropic phase. As the LCE fiber contracts in the illumination zone, the corresponding tensile force increases. Considering that only a portion of the LCE fiber is exposed to illumination, this leads to an uneven distribution of tension in the LCE fiber. In this case, the stretch rates of segments ABC and ADC are λ_1 and λ_2, and this imbalance encourages the LCE fiber to move under tension.

Furthermore, wheels 1 and 2 rotate under the torque formed by the two different tensile forces. The tension in segment ABC is denoted by F_1, and the tension in segment ADC is denoted by F_2. To make the two wheels rotate in the same direction, two coordinating wheels 3 and 4 with both radii r_1 are added and connected by winding them with an elastic cord, as shown in Fig. 1(a). The tension in segment EF is F_3, and the tension in segment GH is F_4. Meanwhile, the centers of these two coordinating wheels coincide with the circular axes of wheels A and B, respectively. With these two coordinating wheels, it is possible to rotate wheels A and B in the same direction. As wheels A and B rotate, different segments of the

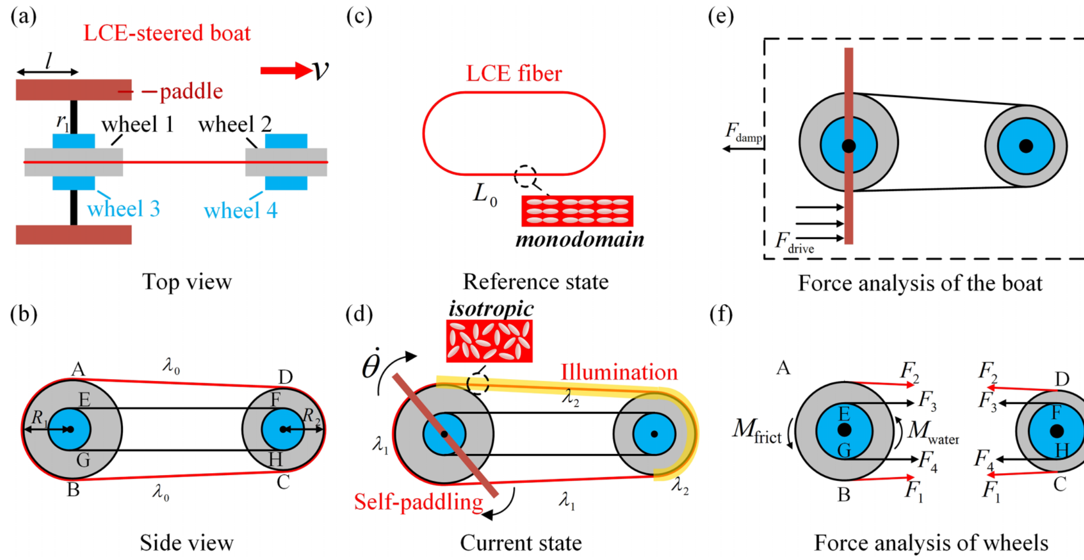

FIG. 1. Schematic diagram of the LCE-based motor in the self-paddling boat system (a) Top view of LCE steered boat; (b) Side view of LCE steered boat; (c) Reference state of the LCE fiber; (d) Current state of the LCE-based motor; (e) Force analysis of the boat; (f) Force analysis of the wheels. The self-paddling boat system is capable of self-paddling under steady illumination.

LCE fiber enter and leave the illumination zone successively, thus bringing the entire LCE-based motor into a dynamic equilibrium for continuous and stable operation. The installation of paddles on the LCE-based motor enables the boat to self-paddle.

The boat is subjected to the driving force F_{drive} provided by the action of the water on the paddles and the damping force F_{damp} of the water on the boat, as shown in Fig. 1(e). For steady paddling of the boat, the driving force is balanced with the damping force, i.e.,

$$F_{\text{drive}} = F_{\text{damp}}. \tag{1}$$

The driving force is assumed to be proportional to the relative speed of the paddle relative to the stationary water, i.e.,

$$F_{\text{drive}} = \beta_1(\dot{\theta} l - v), \tag{2}$$

where β^1 refers to the rotational damping coefficient of paddle, $\dot{\theta}$ denotes the angular velocity of wheel 3, l is the length of paddle, and v represents the paddling velocity of the entire LCE-steered boat. The damping force is assumed to be proportional to the paddling velocity of the LCE-steered boat, i.e.,

$$F_{\text{damp}} = \beta_2 v, \tag{3}$$

where β_2 refers to the damping coefficient of boat.

Meanwhile, for steady paddling, wheel 3 is in equilibrium and is subjected to the maximum frictional torque M_{frict}, the driving torque M_{drive}, and the resistance torque M_{water} of water against wheel 3, as shown in Fig. 1(f). The equilibrium equation can be expressed as

$$M_{\text{drive}} - M_{\text{frict}} = M_{\text{water}}, \tag{4}$$

where the resistance torque can be derived as

$$M_{\text{water}} = F_{\text{drive}} l. \tag{5}$$

Combining Eqs. (1)–(5) yields the paddling velocity of the boat:

$$v = \frac{M_{\text{drive}} - M_{\text{frict}}}{\beta_2 l}, \tag{6}$$

and angular velocity of the wheels:

$$\dot{\theta} = \frac{(\beta_1 + \beta_2)(M_{\text{drive}} - M_{\text{frict}})}{\beta_1 \beta_2 l^2}. \tag{7}$$

B. Photothermally driven driving torque of the LCE-based motor

In this section, the photothermally driven driving torque M_{drive} of the LCE-based motor is derived. The force analysis diagram of the LCE-based motor is presented in Fig. 1(f). The torque balance equations for wheels 1 and 2 can be described as

$$(F_1 - F_2)R_1 + (F_4 - F_3)r_1 + M_{\text{drive}} = 0, \tag{8}$$

and

$$(F_2 - F_1)R_2 + (F_3 - F_4)r_1 = 0, \tag{9}$$

where F_1, F_2, F_3, and F_4 represent the tensile forces of segments ABC, ADC, EF, and GH, respectively.

From Eqs. (8) and (9), the driving torque of the LCE-based motor can be written as

$$M_{\text{drive}} = (F_1 - F_2)(R_1 - R_2). \tag{10}$$

The tensile force of the LCE fiber is assumed to be linearly related to its elongation, so that it can be obtained as

$$F_1 = k_L\left(L_I - \frac{L_I}{\lambda_1}\right), \tag{11}$$

and

$$F_2 = k_L\left(L_{II} - \frac{L_{II}}{\lambda_2}\right), \tag{12}$$

where k_L is the elastic coefficient of LCE, and L_I and L_{II} denote the lengths of segments ABC and ADC, respectively.

Substituting Eqs. (11) and (12) into Eq. (10) yields

$$M_{\text{drive}} = \left[k_L\left(L_I - \frac{L_I}{\lambda_1}\right) - k_L\left(L_{II} - \frac{L_{II}}{\lambda_2}\right)\right](R_1 - R_2). \quad (13)$$

The λ_1 and λ_2 in Eq. (13) also need to satisfy the following two conditions. To ensure the stable operation of the LCE-based motor, the amount of LCE on wheel 1 with radius R_1 should be equal to the amount of LCE on wheel 2 with radius R_2 [71]. The above condition can be expressed as

$$\frac{\Delta\theta R_1}{\lambda_1} = \frac{\Delta\theta R_2}{\lambda_2}, \quad (14)$$

where $\Delta\theta$ is the rotation angle.

Meanwhile, to avoid relative sliding of wheels 1 and 2 against the LCE fiber, it is also necessary to ensure that the total length of the LCE fiber remains constant [71], so that we can get another condition:

$$\frac{L_{II}}{(1+\varepsilon_I)\lambda_2} + \frac{L_I}{\lambda_1} = L_0, \quad (15)$$

where L_I and L_{II} are the lengths of segments ABC and ADC, respectively, and ε_I denotes the photothermally driven strain of the LCE fiber, which is related to the temperature change $T(t)$ in the LCE fiber and can be written as

$$\varepsilon_I = -CT(t), \quad (16)$$

where C is the contraction coefficient.

C. Temperature in the LCE fiber

In this section, we will derive the temperature change in the photothermally responsive LCE fiber under steady illumination and dark conditions. In the self-paddling process of the boat, there is heat exchange between the LCE fiber and the surrounding environment. Combined with the experimentally determined values of the heat transfer coefficient $K = 10\ \mathrm{W\,m^{-2}\,K^{-1}}$, the thermal conductivity $h = 0.1\ \mathrm{W\,m^{-1}\,K^{-1}}$, the fiber radius $r = 10^{-5}$ m in the experiments [74–77], and the Biot number $\mathrm{B_i} = Kr/h = 10^{-3}$, it is assumed that the temperature field within the LCE fiber is uniform and identical. Under steady illumination, the temperature of the LCE fiber can be expressed as

$$\frac{\mathrm{d}T}{\mathrm{d}t} = \frac{q - KT}{\rho_C}, \quad (17)$$

where ρ_C is the specific heat capacity, and q represents the heat flux from the steady illumination.

For Case I that the LCE fiber is in the illumination state switched from the dark state with transient temperature T_{dark}, by solving Eq. (17), the temperature T in the LCE fiber is

$$T(t) = T_{\text{dark}} + \frac{q}{K}\left[1 - \exp\left(-\frac{t_1}{\tau}\right)\right], \quad (18)$$

where $\tau = \frac{\rho_C}{K}$ indicates the thermal characteristic time, and t_1 is the duration of current process.

For Case II that the LCE fiber is in the dark state (i.e., $q = 0$) switched from the illumination state with transient temperature T_{illum}, the temperature T in the LCE fiber can be derived from Eq. (17) as

$$T(t) = T_{\text{illum}} \exp\left(-\frac{t_2}{\tau}\right), \quad (19)$$

where t_2 is the duration of current process.

It is noted that recent experiments have shown that the thermal characteristic time of the LCE fiber to photothermal stimulation is <0.1 s, and several instances of self-oscillations have been successfully showcased [6,61]. For simplicity, we assumed that the thermal characteristic time is much smaller than the rotation period of the LCE-based motor, i.e., τ is assumed to be infinitely ∼0. Then Eq. (18) for the illumination zone can be reduced to

$$T_{\text{illum}} = T_{\text{dark}} + \frac{q}{K}. \quad (20)$$

Equation (19) for the dark zone can be derived as

$$T_{\text{dark}} = 0. \quad (21)$$

D. Nondimensionalization

For computational convenience, the following dimensionless parameters are introduced: $\bar{L}_0 = \frac{L_0}{R_2}$, $\bar{L} = \frac{L}{R_2}$, $\bar{R}_1 = \frac{R_1}{R_2}$, $\bar{L}_I = \frac{L_I}{R_2}$, $\bar{L}_{II} = \frac{L_{II}}{R_2}$, $\bar{l} = \frac{l}{R_2}$, $\bar{F}_1 = \frac{F_1}{mg}$, $\bar{F}_2 = \frac{F_2}{mg}$, $\bar{F}_3 = \frac{F_3}{mg}$, $\bar{F}_4 = \frac{F_4}{mg}$, $\bar{M}_{\text{drive}} = \frac{M_{\text{drive}}}{mgR_2}$, $\bar{M}_{\text{frict}} = \frac{M_{\text{frict}}}{mgR_2}$, $\bar{\dot{\theta}} = \dot{\theta}\tau$, $\bar{v} = \frac{v}{\tau g}$, $\bar{k}_L = \frac{k_L R_2}{mg}$, $\bar{C} = CT_A$, $\bar{\beta}_1 = \frac{\beta_1\tau}{m}$, $\bar{\beta}_2 = \frac{\beta_2\tau}{m}$, $\bar{T} = \frac{T}{T_A}$ (T_A is ambient temperature), $\bar{T}_{\text{illum}} = \frac{T_{\text{illum}}}{T_A}$, and $\bar{q} = \frac{q}{KT_A}$. Thus, the dimensionless form of Eq. (13) can be written as

$$\bar{M}_{\text{drive}} = \left[\bar{k}_L\left(\bar{L}_I - \frac{\bar{L}_I}{\lambda_1}\right) - \bar{k}_L\left(\bar{L}_{II} - \frac{\bar{L}_{II}}{\lambda_2}\right)\right](\bar{R}_1 - 1). \quad (22)$$

Then the dimensionless form of Eq. (14) can be written as

$$\lambda_1 = \lambda_2 \bar{R}_1. \quad (23)$$

Furthermore, the dimensionless form of Eq. (15) can be written as

$$\frac{\bar{L}_{II}}{(1+\varepsilon_I)\lambda_2} + \frac{\bar{L}_I}{\lambda_1} = \bar{L}_0. \quad (24)$$

For the illumination zone, Eq. (20) can be rewritten as

$$\bar{T}_{\text{illum}} = \bar{q}. \quad (25)$$

By combing Eqs. (6), (7), (16), and (22)–(25), we can obtain the dimensionless angular velocity:

$$\bar{v} = \frac{\left[\bar{k}_L\left(\bar{L}_I - \frac{\bar{L}_I}{\lambda_1}\right) - \bar{k}_L\left(\bar{L}_{II} - \frac{\bar{L}_{II}}{\lambda_2}\right)\right](\bar{R}_1 - 1) - \bar{M}_D}{\bar{\beta}_2 \bar{l}}, \quad (26)$$

and paddling velocity:

$$\bar{\dot{\theta}} = \frac{(\bar{\beta}_1 + \bar{\beta}_2)}{\bar{\beta}_1 \bar{l}} \frac{\left[\bar{k}_L\left(\bar{L}_I - \frac{\bar{L}_I}{\lambda_1}\right) - \bar{k}_L\left(\bar{L}_{II} - \frac{\bar{L}_{II}}{\lambda_2}\right)\right](\bar{R}_1 - 1) - \bar{M}_D}{\bar{\beta}_2 \bar{l}}. \quad (27)$$

Substituting the dimensionless system parameters including the maximum frictional torque $\bar{M}_D$, the heat flux $\bar{q}$, contraction coefficient C, the original length $\bar{L}_0$, and initial stretch rate λ_0 of the LCE fiber, the wheel 1 radius $\bar{R}_1$, the length of paddle $\bar{l}$, the rotational damping coefficient $\bar{\beta}_1$ of

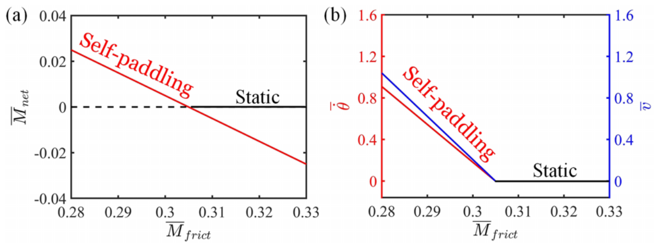

FIG. 2. Effect of maximum frictional torque $\bar{M}_{\text{frict}}$ on (a) net driving torque $\bar{M}_{\text{net}}$ and (b) angular velocity of the wheel and paddling velocity of the LCE-steered boat. A critical maximum frictional torque of $\bar{M}_{\text{frict}} = 0.305$ exists for triggering the self-paddling. An increase in the maximum frictional torque $\bar{M}_{\text{frict}}$ leads to a decline in the angular velocity and paddling velocity of the self-paddling.

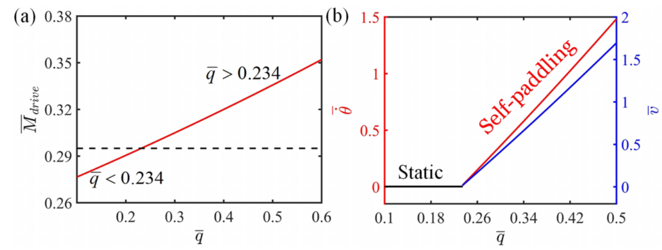

FIG. 3. Effect of heat flux $\bar{q}$ on (a) driving torque $\bar{M}_{\text{drive}}$ and (b) angular velocity of the wheel and paddling velocity of the LCE-steered boat. A threshold value of $\bar{q} = 0.234$ for heat flux to trigger the self-paddling is witnessed. As the heat flux increases, both the angular velocity and paddling velocity of the self-paddling undergo gradual increments.

paddle, the damping coefficient $\bar{\beta}_2$ of boat, and the elastic coefficient $\bar{k}_{\text{L}}$ of the LCE fiber into Eqs. (26) and (27), the paddling velocity of the LCE-steered boat and the angular velocity of the wheels can be obtained.

III. RESULTS AND DISCUSSIONS

From Eqs. (26) and (27), it can be seen that the angular velocity and paddling velocity depends on the following parameters: the maximum frictional torque $\bar{M}_{\text{frict}}$, the heat flux $\bar{q}$, contraction coefficient C, the initial stretch rate λ_0, the wheel 1 radius $\bar{R}_1$, the length of paddle $\bar{l}$, the rotational damping coefficient $\bar{\beta}_1$ of paddle, the damping coefficient $\bar{\beta}_2$ of boat, and the elastic coefficient $\bar{k}_{\text{L}}$ of the LCE fiber. This section will conduct a quantitative analysis on the effects of these system parameters on both the angular velocity $\bar{\dot{\theta}}$ of the wheel and the paddling velocity of the LCE-steered boat $\bar{v}$.

A. Effect of maximum frictional torque on self-paddling

This section discusses the effect of maximum frictional torque $\bar{M}_{\text{frict}}$ on the self-paddling of the LCE-steered boat, where the other dimensionless parameters are $\bar{q} = 0.3$, $C = 0.4$, $\bar{L}_0 = 20$, $\lambda_0 = 1.3$, $\bar{R}_1 = 1.2$, $\bar{l} = 1.2$, $\bar{\beta}_1 = 0.4$, $\bar{\beta}_2 = 0.02$, and $\bar{k}_{\text{L}} = 7$. Fig. 2(a) illustrates the relationship between the maximum frictional torque $\bar{M}_{\text{frict}}$ and the net driving torque $\bar{M}_{\text{net}} = \bar{M}_{\text{drive}} - \bar{M}_{\text{frict}}$. It is evident that, as the maximum frictional torque increases, the net driving torque decreases continuously. When the net driving torque drops <0, i.e., when the maximum frictional torque >0.305, the LCE-based motor fails to operate. A negative net driving torque indicates that the torque generated by the tension of the LCE fiber in the motor is not sufficient to overcome the frictional torque of the wheel, thus preventing the wheel from turning. Conversely, when the net driving torque is >0, i.e., when the maximum frictional torque is <0.305, the LCE-based motor can operate. A positive net driving torque indicates that the torque generated by the tension of the LCE fiber can overcome the frictional torque of the wheel, thus turning the wheel. The impact of the maximum frictional torque on the angular velocity of the wheel and the paddling velocity of the LCE-steered boat can be observed in Fig. 2(b). When the maximum frictional torque surpasses 0.305, the LCE-based motor operates in the static mode. On the contrary, when the maximum frictional torque falls <0.305, the LCE-based motor switches to the self-paddling mode. As the maximum frictional torque continues to increase, the angular velocity of the wheel and the paddling velocity of the LCE-steered boat show monotonical decrements.

B. Effect of heat flux on self-paddling

The effect of heat flux on the self-paddling is investigated in current section, and the other dimensionless parameters are selected as $\bar{M}_{\text{frict}} = 0.295$, $C = 0.4$, $\bar{L}_0 = 20$, $\lambda_0 = 1.3$, $\bar{R}_1 = 1.2$, $\bar{l} = 1.2$, $\bar{\beta}_1 = 0.4$, $\bar{\beta}_2 = 0.02$, and $\bar{k}_{\text{L}} = 7$. Fig. 3(a) gives the values of driving torque for different heat flux, where the black dashed line represents the maximum frictional torque. With the increase in heat flux, the driving torque experiences a continuous increase. The impacts of heat flux on the angular velocity of the wheel and the paddling velocity of the LCE-steered boat are presented in Fig. 3(b). A threshold value for mode transition is witnessed. When the heat flux is <0.234, the system is in the static mode. Conversely, when the heat flux is >0.234, the system is in the self-paddling mode. When the heat flux is low, less energy is absorbed by the LCE fiber, resulting in a lower tensile force in the LCE fiber and thus producing a lower driving torque, which is not enough to counteract the maximum frictional torque and initiate rotation of the LCE-based motor. Otherwise, as the heat flux increases continuously, more energy is absorbed by the LCE fiber, which can generate a higher tensile force and greater driving torque, leading to faster wheel rotation and an increase in both the angular velocity of the wheel and the paddling velocity of the boat.

C. Effect of contraction coefficient on self-paddling

The present section investigates the influence of contraction coefficient on the self-paddling, while keeping the other dimensionless parameters as $\bar{M}_{\text{frict}} = 0.295$, $\bar{q} = 0.3$, $\bar{L}_0 = 20$, $\lambda_0 = 1.3$, $\bar{R}_1 = 1.2$, $\bar{l} = 1.2$, $\bar{\beta}_1 = 0.4$, $\bar{\beta}_2 = 0.02$, and $\bar{k}_{\text{L}} = 7$. In Fig. 4(a), the variation of the driving torque under different contraction coefficients is depicted, with the black dashed line representing the maximum frictional torque. The driving torque increases continuously with the increase of the contraction coefficient. Fig. 4(b) demonstrates the impacts of contraction coefficient on the angular velocity of the wheel

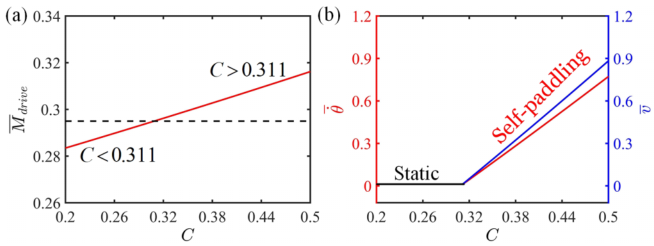

FIG. 4. Effect of contraction coefficient C on (a) driving torque $\bar{M}_{\text{drive}}$ and (b) angular velocity of the wheel and paddling velocity of the LCE-steered boat. A critical contraction coefficient of $C = 0.311$ is observed to be responsible for initiating the self-paddling. In addition, an increment in the contraction coefficient leads to an increase in both the angular velocity and paddling velocity of the self-paddling.

and the paddling velocity of the LCE-steered boat. A critical contraction coefficient of $C = 0.311$ is observed to be responsible for the mode transition. Specifically, the system is in the static mode when the contraction coefficient is <0.311. In contrast, the system switches to the self-paddling mode when the contraction coefficient surpasses 0.311. When the contraction coefficient is low, the LCE fiber is less efficient at utilizing the light energy, resulting in a lower tensile force within the LCE fiber, which in turn generates a lower driving torque. This lower torque is insufficient to counteract the maximum frictional torque, thereby impeding the initiation of rotation in the LCE-based motor. Conversely, as the contraction coefficient increases, the efficiency of the LCE fiber in utilizing the light energy improves, leading to an increase in the tensile force and a subsequent enhancement of the driving torque. As a result, both the angular velocity of the wheel and the paddling velocity of the LCE-steered boat exhibit a gradual incremental behavior.

D. Effect of initial stretch rate on self-paddling

The current section examines the influence of different initial stretch rates on the self-paddling, with the remaining parameters being set to $\bar{M}_{\text{frict}} = 0.295$, $\bar{q} = 0.3$, $C = 0.4$, $\bar{L}_0 = 20$, $\bar{R}_1 = 1.2$, $\bar{l} = 1.2$, $\bar{\beta}_1 = 0.4$, $\bar{\beta}_2 = 0.02$, and $\bar{k}_{\text{L}} = 7$. Displaying the values of the driving torque under varying initial stretch rates, Fig. 5(a) indicates that the higher the initial stretch rate, the higher the driving torque. Fig. 5(b) depicts the effect of initial stretch rate on the angular velocity of the wheel and the paddling velocity of the LCE-steered boat. A threshold value, referred to as 1.282, is witnessed, distinguishing between the static mode and the self-paddling mode. When the initial stretch rate is <1.282, the system remains in the static mode. However, once the initial stretch rate >1.282, the system enters the self-paddling mode. In the self-paddling mode, an increase in the stretch rate induces a corresponding rise in both the angular velocity and the paddling velocity, as shown in Fig. 5(b). With a small initial stretch rate <1.282, the LCE fiber produces lower tensile force and is unable to yield sufficient driving torque to overcome the maximum frictional torque, thus the wheel cannot rotate. Conversely, as the initial stretch rate progressively increases and approaches 1.282, the driving torque exceeds the maximum frictional torque threshold, and the system enters the self-paddling mode. With the further increment of the initial stretch rate, the driving torque of the LCE-based motor continues to increase, causing the wheel to accelerate the rotation, and consequently, the angular velocity and paddling velocity increase as well.

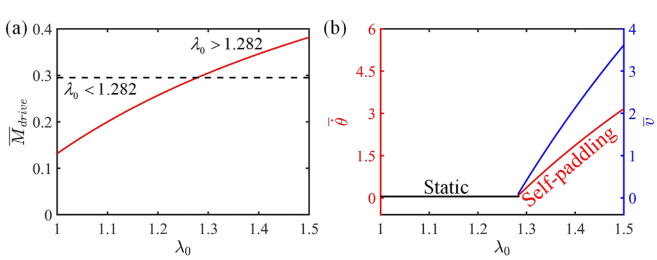

FIG. 5. Effect of initial stretch rate λ_0 on (a) driving torque $\bar{M}_{\text{drive}}$ and (b) angular velocity of the wheel and paddling velocity of the LCE-steered boat. A critical initial stretch rate of $\lambda_0 = 1.282$ is present to trigger the self-paddling. Moreover, when raising the initial stretch rate, both the angular velocity and paddling velocity of the self-paddling exhibit an increase.

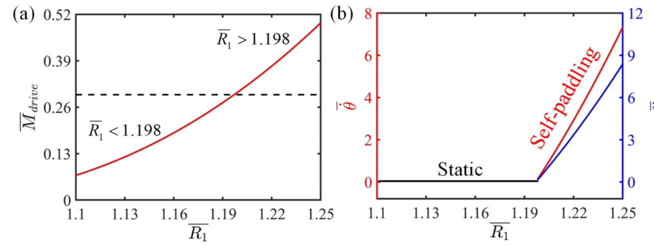

FIG. 6. Effect of radius $\bar{R}_1$ of wheel 1 on (a) driving torque $\bar{M}_{\text{drive}}$ and (b) angular velocity of the wheel and paddling velocity of the LCE-steered boat. The self-paddling mode is triggered when $\bar{R}_1$ reaches 1.198. Furthermore, a larger $\bar{R}_1$ corresponds to an increase in both the angular velocity and paddling velocity of the self-paddling.

E. Effect of wheel radius $\bar{R}_1$ on self-paddling

The effect of diverse $\bar{R}_1$ on the self-paddling is explored in this section, with the other parameters held constant at $\bar{M}_{\text{frict}} = 0.295$, $\bar{q} = 0.3$, $C = 0.4$, $\bar{L}_0 = 20$, $\lambda_0 = 1.3$, $\bar{l} = 1.2$, $\bar{\beta}_1 = 0.4$, $\bar{\beta}_2 = 0.02$, and $\bar{k}_{\text{L}} = 7$. Fig. 6(a) displays the driving torque as a function of $\bar{R}_1$, with the black dashed line denoting the maximum frictional torque. As $\bar{R}_1$ increases, the driving torque shows a gradual incremental behavior. The variation curves of the angular velocity and paddling velocity with $\bar{R}_1$ are depicted in Fig. 6(b). It is obvious that there exists a threshold value of $\bar{R}_1$, i.e., 1.198, which differentiates between the static mode and the self-paddling mode. Specifically, when $\bar{R}_1 < 1.198$, the system operates in the static mode, and when $\bar{R}_1 > 1.198$, the system transitions to the self-paddling mode. A small $\bar{R}_1 < 1.198$ means that there is not much difference between the radii of wheels 1 and 2. This results in the tensile forces of segments ABC and ADC in the LCE fiber being close to each other, which produces a small driving torque which cannot drive the wheel. In contrast, as $\bar{R}_1$ gradually increases and approaches 1.198, a larger radius difference is formed between wheels 1 and 2, which induces a larger tension difference between segments ABC and ADC, thus

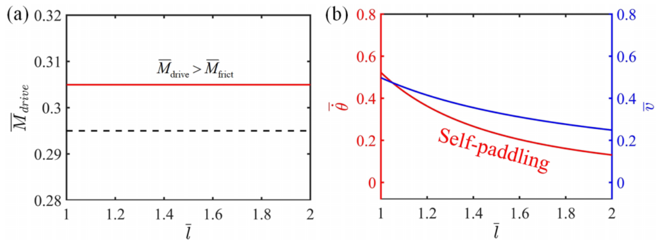

FIG. 7. Effect of paddle length $\bar{l}$ on (a) driving torque $\bar{M}_{\rm drive}$ and (b) angular velocity of the wheel and paddling velocity of the LCE-steered boat. An increase in the paddle length leads to a gradual decrease in both the angular velocity and paddling velocity of the self-paddling boat.

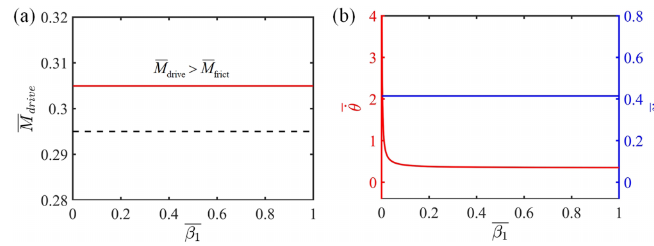

FIG. 8. Effect of rotational damping coefficient $\bar{\beta}_1$ of paddle on (a) driving torque $\bar{M}_{\rm drive}$ and (b) angular velocity of the wheel and paddling velocity of the LCE-steered boat. As the damping coefficient of paddle increases, the angular velocity of the self-paddling decreases, while the velocity of boat is unchanged.

generating a larger driving torque, and furthermore, increasing the angular velocity of the wheel and the paddling velocity of the boat.

F. Effect of paddle length on self-paddling

This section focuses on the impact of paddle length on the self-paddling, with $\bar{M}_{\rm frict} = 0.295$, $\bar{q} = 0.3$, $C = 0.4$, $\bar{L}_0 = 20$, $\lambda_0 = 1.3$, $\bar{R}_1 = 1.2$, $\bar{\beta}_1 = 0.4$, $\bar{\beta}_2 = 0.02$, and $\bar{k}_{\rm L} = 7$. The values of the driving torque for different paddle lengths are displayed in Fig. 7(a), where the black dashed line represents the maximum frictional torque. The driving torque always exceeds the maximum frictional torque, indicating the maintenance of the system in the self-paddling mode. The variation in paddle length does not alter the driving torque because the driving torque is determined solely by the tensile force of the LCE fiber inside the motor and the radii of wheels 1 and 2, independent of the paddle length. Fig. 7(b) depicts the influence of paddle length on the angular velocity of the wheel and the paddling velocity of the LCE-steered boat. It is obvious that the system consistently operates in the self-paddling mode. Moreover, as the paddle length increases, both the angular velocity and the paddling velocity decrease. With the increment in paddle length, the LCE-based motor experiences an increased resistance torque from the water, which in turn reduces the angular velocity of the wheel. At the same time, a reduction in the angular velocity of the wheel reduces the output power of the LCE-based motor, which in turn inhibits the paddling velocity of the boat.

G. Effect of rotational damping coefficient of paddle on self-paddling

The current section investigates how the rotational damping coefficients of paddle influences the self-paddling, with the rest of the parameters set to $\bar{M}_{\rm frict} = 0.295$, $\bar{q} = 0.3$, $C = 0.4$, $\bar{L}_0 = 20$, $\lambda_0 = 1.3$, $\bar{R}_1 = 1.2$, $\bar{l} = 1.2$, $\bar{\beta}_2 = 0.02$, and $\bar{k}_{\rm L} = 7$. As plotted in Fig. 8(a), the driving torque remains constant and always surpasses the maximum frictional torque, which clearly indicates that the system is sustained in the self-paddling mode. Owing to the complete dependence of the driving torque on the tensile force and stretching of the LCE fiber, the rotational damping coefficient of the paddle has no effect on the driving torque. Fig. 8(b) describes the effect of rotational damping coefficient of the paddle on both the angular velocity of the wheel and the paddling velocity of the LCE-steered boat. The system always operates in the self-paddling mode. Furthermore, as the rotational damping coefficient of the paddle increases, the angular velocity decreases, while the paddling velocity remains constant. The increased damping coefficient of the paddle induces a larger resistance torque applied to the rotation of the paddle, and therefore, the angular velocity of the LCE-based motor decreases. Conversely, the overall force acting on the boat is entirely determined by the resistance force on the paddles. Hence, increasing the damping coefficient of the paddle will not affect the external frictional torque on the boat and therefore, as a consequence, will not alter the paddling velocity of the boat.

H. Effect of rotational damping coefficient of boat on self-paddling

How the rotational damping coefficients of paddle affects the self-paddling is examined in this section, while keeping other parameters constant at $\bar{M}_{\rm frict} = 0.295$, $\bar{q} = 0.3$, $C = 0.4$, $\bar{L}_0 = 20$, $\lambda_0 = 1.3$, $\bar{R}_1 = 1.2$, $\bar{l} = 1.2$, $\bar{\beta}_1 = 0.4$, and $\bar{k}_{\rm L} = 7$. In Fig. 9(a), the driving torque values for different damping coefficients of paddle are presented, with the black dashed line referring to the maximum frictional torque. The always higher driving torque than the maximum frictional torque clearly shows the system always adheres to the self-paddling mode. In addition, the driving torque remains unaffected by variations in the damping coefficients of the paddle, as it is solely governed by the tensile force of the LCE fiber and the radii of wheels 1 and 2. The impact of the damping coeffi-

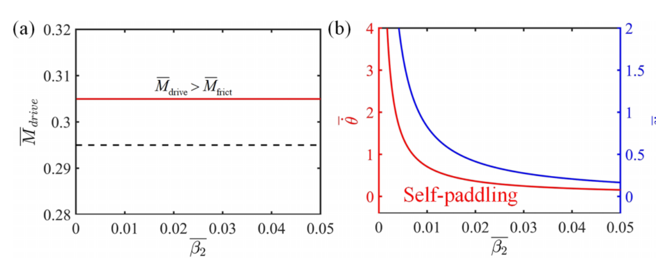

FIG. 9. Effect of rotational damping coefficient $\bar{\beta}_2$ of boat on (a) driving torque $\bar{M}_{\rm drive}$ and (b) angular velocity of the wheel and paddling velocity of the LCE-steered boat. With the increase in the rotational damping coefficient of boat, both the angular velocity and paddling velocity of the self-paddling boat undergo gradual declines.

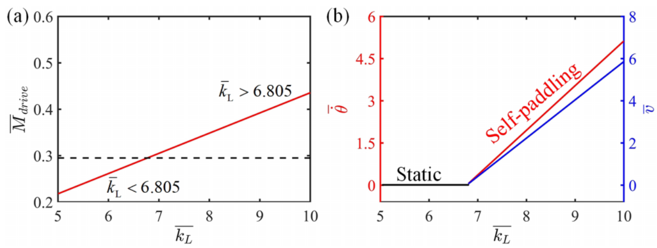

FIG. 10. Effect of elastic coefficient $\bar{k}_{\rm L}$ of LCE fiber on (a) driving torque $\bar{M}_{\rm drive}$ and (b) angular velocity of the wheel and paddling velocity of the LCE-steered boat. Self-paddling is initiated at a critical elastic coefficient of $\bar{k}_{\rm L} = 6.802$. Furthermore, the increase in elastic coefficient of the LCE fiber results in a simultaneous increase in both the angular velocity and paddling velocity of the self-paddling boat.

cient of the boat on the angular velocity of the wheel and the paddling velocity of the LCE-steered boat is displayed in Fig. 9(b). The figure clearly shows that the system is always in the self-paddling mode. Moreover, with the increase in the rotational damping coefficient of boat, both the angular velocity and paddling velocity of the self-paddling boat undergo gradual declines. The larger the damping coefficient of boat, the larger the resistance arm experienced by the boat from the water and thereby the greater water-induced resistance torque, which ultimately induces a decrement in the paddling velocity of the boat.

I. Effect of elastic coefficient of LCE fiber on self-paddling

In this section, we explore the impact of the elastic coefficient of the LCE fiber on the self-paddling, with other parameters being $\bar{M}_{\rm frict} = 0.295$, $\bar{q} = 0.3$, $C = 0.4$, $\bar{L}_0 = 20$, $\lambda_0 = 1.3$, $\bar{R}_1 = 1.2$, $\bar{l} = 1.2$, $\bar{\beta}_1 = 0.4$, and $\bar{\beta}_2 = 0.02$. In Fig. 10(a), the values of driving torque under varying elastic coefficients of the LCE fiber are provided, with the black dashed line representing the maximum frictional torque. With the increasing elastic coefficient, the driving torque experiences a monotonical increment. Fig. 10(b) demonstrates how the elastic coefficient affects the angular velocity of the wheel and the paddling velocity of the LCE-steered boat. A critical elastic coefficient of 6.805 exists for the mode transition. Specifically, when the elastic coefficient is <6.805, the system operates in the static mode, and when the elastic coefficient surpasses 6.805, the system switches to the self-paddling mode. For a smaller elastic coefficient <6.805, the LCE fiber produces less elastic force as it contracts under illumination and consequently generates less driving torque. This lower driving torque is not sufficient to counteract the maximum frictional torque, which impedes the LCE-based motor from starting to rotate. As the elastic coefficient increases, the LCE fiber produces a greater elastic force as it contracts under illumination, which brings about a subsequent enhancement of the driving torque. As a result, both the angular velocity and the paddling velocity of the self-paddling boat increase.

Here, the effects of some key system parameters on the angular velocity and paddling velocity are summarized in Table I. These results are instructive for the design of self-paddling system and the regulation of self-paddling behaviors.

IV. CONCLUSIONS

Conventional control approaches for active machines, such as sensor control and external device control, have proven to be complex and challenging to implement in an effective manner. In contrast, active materials–based self-oscillators offer distinct benefits, including periodic motion and ease of regulation, and thereby hold great promise for various applications. Inspired by paddle boats, we proposed a conceptual light-fueled self-paddling boat with a photothermally responsive LCE-based motor, and the self-paddling boat can achieve continuous forward motion under steady illumination. Combining the well-established dynamic LCE model and rotation dynamics, we have derived the governing equations for the self-paddling motion and formulated the driving torque of the LCE-based motor and the paddling velocity of the LCE-steered boat. The results show the existence of two different motion modes for the LCE-steered boat under steady illumination: the static mode and the self-paddling mode. The self-paddling mode is originated from the competition between the light-fueled driving torque and the frictional torque.

Moreover, we have conducted a quantitative investigation into the critical conditions required to initiate the self-paddling mode as well as a detailed examination of the system parameters influencing the driving torque, angular velocity, and paddling velocity. Increasing the system parameters including the heat flux $\bar{q}$, the contraction coefficient C, the initial stretch rate λ_0, the wheel radius $\bar{R}_1$, and the elastic coefficient of the LCE fiber $\bar{k}_{\rm L}$ will bring about an increase in the paddling velocity. Conversely, the increases in the maximum frictional torque $\bar{M}_{\rm frict}$, the paddle length $\bar{l}$, and the rotational

TABLE I. Effects of parameters on angular velocity and paddling velocity.

Parameter	Angular velocity	Paddling velocity
$\bar{M}_{\rm frict}$	Decreases with increasing $\bar{M}_{\rm frict}$	Decreases with increasing $\bar{M}_{\rm frict}$
$\bar{q}$	Increases with increasing $\bar{q}$	Increases with increasing $\bar{q}$
C	Increases with increasing C	Increases with increasing C
λ_0	Increases with increasing λ_0	Increases with increasing λ_0
$\bar{R}_1$	Increases with increasing $\bar{R}_1$	Increases with increasing $\bar{R}_1$
$\bar{l}$	Decreases with increasing $\bar{l}$	Decreases with increasing $\bar{l}$
$\bar{\beta}_1$	Decreases with increasing $\bar{\beta}_1$	Slightly affected by $\bar{\beta}_1$
$\bar{\beta}_2$	Decreases with increasing $\bar{\beta}_2$	Decreases with increasing $\bar{\beta}_2$
$\bar{k}_{\rm L}$	Increases with increasing $\bar{k}_{\rm L}$	Increases with increasing $\bar{k}_{\rm L}$

damping coefficient of paddle $\bar{\beta}_1$ will induce a decrease in the paddling velocity of the boat. The conceptual self-paddling boat proposed in this paper based on the LCE-based motor has unique advantages, for instances, customizable size, and being untethered and ambient powered, all of which render it a highly practical value in the design and implementation of micromachines, soft robotics, and energy harvesters.

ACKNOWLEDGMENTS

This paper was funded by University Natural Science Research Project of Anhui Province (Grant No. 2022AH020029), National Natural Science Foundation of China (Grant No. 12172001), and Anhui Provincial Natural Science Foundation (Grants No. 2008085QA23 and No. 2208085Y01).

[1] M. Behl and A. Lendlein, Actively moving polymers, Soft Matter **3**, 58 (2007).
[2] F. Ciardelli, O. Pieroni, A. Fissi, C. Carlini, and A. Altomare, Photoresponsive optically active polymers-a review, Br. Polym. J. **21**, 97 (1989).
[3] T. White and D. Broer, Programmable and adaptive mechanics with liquid crystal polymer networks and elastomers, Nat. Mater. **14**, 1087 (2015).
[4] T. Qazi, R. Rai, and A. Boccaccini, Tissue engineering of electrically responsive tissues using polyaniline based polymers: A review, Biomaterials **35**, 9068 (2014).
[5] S. Namathoti, R. V. M., and R. P. S., A review on progress in magnetic, microwave, ultrasonic responsive Shape-memory polymer composites, Mater. Today: Proc. **56**, 1182 (2022).
[6] Q. He, Z. Wang, Y. Wang, Z. Wang, C. Li, R. Annapooranan, J. Zeng, R. Chen, and S. Cai, Electrospun liquid crystal elastomer microfiber actuator, Sci. Robot. **6**, eabi9704 (2021).
[7] V. Sangwan, A. Taneja, and S. Mukherjee, Design of a robust self-excited biped walking mechanism, Mech. Mach. Theory **39**, 1385 (2004).
[8] M. Wehner, R. L. Truby, D. J. Fitzgerald, B. Mosadegh, G. M. Whitesides, J. A. Lewis, and R. J. Wood, An integrated design and fabrication strategy for entirely soft, autonomous robots, Nature (London) **536**, 451 (2016).
[9] Q. He, R. Yin, Y. C. Hua, W. J. Jiao, C. Y. Mo, H. Shu, and J. R. Raney, A modular strategy for distributed, embodied control of electronics-free soft robots, Sci. Adv. **9**, eade9247 (2023).
[10] Y. Zhao, Y. Chi, Y. Hong, Y. Li, Y. Shu, and J. Yin, Twisting for soft intelligent autonomous robot in unstructured environments, Proc. Natl. Acad. Sci. USA **119**, e2200265119 (2022).
[11] G. Vantomme, A. H. Gelebart, D. J. Broer, and E. W. Meijer, four-blade light-driven plastic mill based on hydrazone liquid-crystal networks, Tetrahedron **73**, 4963 (2017).
[12] B. Liao, H. Zang, M. Chen, Y. Wang, X. Lang, N. Zhu, Z. Yang, and Y. Yi, Soft rod-climbing robot inspired by winding locomotion of snake, Soft Robot. **7**, 500 (2020).
[13] V. V. Yashin and A. C. Balazs, Pattern formation and shape changes in self-oscillating polymer gels, Science **314**, 798 (2006).
[14] X. He, M. Aizenberg, O. Kuksenok, L. D. Zarzar, A. Shastri, A. C. Balazs, and J. Aizenberg, Synthetic homeostatic materials with chemo-mechano-chemical self-regulation, Nature (London) **487**, 214 (2012).
[15] J. Boissonade and P. D. Kepper, Multiple types of spatio-temporal oscillations induced by differential diffusion in the Landolt reaction, Phys. Chem. Chem. Phys. **13**, 4132 (2011).
[16] K. Li, P. Y. Wu, and S. Q. Cai, Chemomechanical oscillations in a responsive gel induced by an autocatalytic reaction, J. Appl. Phys. **116**, 043523 (2014).
[17] S. Anton and H. Sodano, A review of power harvesting using piezoelectric materials, Smart Mater. Struct. **16**, R1 (2007).
[18] T. Tadaki, K. Otsuka, and K. Shimizu, Shape memory alloys, Annu. Rev. Mater. Sci. **18**, 25 (1988).
[19] M. Lahikainen, H. Zeng, and A. Priimagi, Reconfigurable photoactuator through synergistic use of photochemical and photothermal effects, Nat. Commun. **9**, 4148 (2018).
[20] Y. Wang, R. Yin, L. Jin, M. Liu, Y. Gao, J. Raney, and S. Yang, 3D-Printed photoresponsive liquid crystal elastomer composites for free-form actuation, Adv. Funct. Mater. **33**, 2210614 (2023).
[21] Y. Wang, A. Dang, Z. Zhang, R. Yin, Y. Gao, L. Feng, and S. Yang, Repeatable and reprogrammable shape morphing from photoresponsive gold nanorod/liquid crystal elastomers, Adv. Mater. **32**, 2004270 (2020).
[22] H. Wu, C. Zhao, Y. Dai, and K. Li, Light-fueled self-fluttering aircraft with a liquid crystal elastomer-based engine, Commun. Nonlinear. Sci. **132**, 107942 (2024).
[23] R. Kularatne, H. Kim, J. Boothby, and T. Ware, Liquid crystal elastomer actuators: Synthesis, alignment, and applications, J. Polym. Sci. Pol. Phys. **55**, 395 (2017).
[24] Z. Xia, Z. Deng, B. Fang, Y. Yang, and F. Sun, A review on sensory perception for dexterous robotic manipulation, Int. J. Robo. Res. **19**, 2 (2022).
[25] D. Kim, S.-H. Kim, T. Kim, B. B. Kang, M. Lee, W. Park, S. Ku, D. Kim, J. Kwon, H. Lee *et al.*, Review of machine learning methods in soft robotics, PLoS One **16**, e0246102 (2021).
[26] H. Chiel, L. Ting, Ö. Ekeberg, and M. Hartmann, The brain in its body: Motor control and sensing in a biomechanical context, J. Neurosci. **29**, 12807 (2009).
[27] B. Han, Z. Ma, Y. Zhang, L. Zhu, H. Fan, B. Bai, Q. Chen, G. Yang, and H. Sun, Reprogrammable soft robot actuation by synergistic magnetic and light fields, Adv. Funct. Mater **32**, 2110997 (2022).
[28] P. Rothemund, A. Ainla, L. Belding, D. J. Preston, S. Kurihara, Z. G. Suo, and G. Whitesides, A soft, bistable valve for autonomous control of soft actuators, Sci. Robot. **3**, eaar7986 (2018).
[29] D. J. Preston, H. J. Jiang, V. Sanchez, P. Rothemund, J. Rawson, M. P. Nemitz, W. K. Lee, Z. G. Suo, C. J. Walsh, and G. M. Whitesides, A soft ring oscillator, Sci. Robot. **4**, eaaw5496 (2019).
[30] W. Ding, *Self-Excited Vibration* (Springer, Berlin, 2009).
[31] X. Lu, H. Zhang, G. Fei, B. Yu, X. Tong, H. Xia, and Y. Zhao, Liquid-crystalline dynamic networks doped with gold nanorods showing enhanced photocontrol of actuation, Adv. Mater. **30**, 1706597 (2018).
[32] K. Kruse and F. Jülicher, Oscillations in cell biology, Curr. Opin. Cell Biol. **17**, 20 (2005).

[33] R. Yoshida, Evolution of self-oscillating polymer gels as autonomous soft actuators, *Soft Actuators*, edited by K. Asaka and H. Okuzaki (Springer, Singapore, 2019), pp. 61–80.
[34] S. Chatterjee, Self-excited oscillation under nonlinear feedback with time-delay, J. Sound Vib. **330**, 1860 (2011).
[35] S. Serak, N. Tabiryan, R. Vergara, T. J. White, R. A. Vaia, and T. Bunning, Liquid crystalline polymer cantilever oscillators fueled by light, Soft Matter. **6**, 779 (2010).
[36] H. Zeng, M. Lahikainen, L. Liu, Z. Ahmed, O. M. Wani, M. Wang, and A. Priimagi, Light-fuelled freestyle self-oscillators, Nat. Commun. **10**, 5057 (2019).
[37] T. J. White, N. V. Tabiryan, S. V. Serak, U. A. Hrozhyk, V. P. Tondiglia, H. Koerner, R. A. Vaiaa, and T. J. Bunning, A high frequency photodriven polymer oscillator, Soft Matter. **4**, 1796 (2008).
[38] M. Zadan, D. Patel, A. Sabelhaus, J. Liao, A. Wertz, L. Yao, and C. Majidi, Liquid crystal elastomer with integrated soft thermoelectrics for shape memory actuation and energy harvesting, Adv. Mater. **34**, 2200857 (2022).
[39] D. Zhao and Y. Liu, Photomechanical vibration energy harvesting based on liquid crystal elastomer cantilever, Smart. Mater. Struct. **28**, 075017 (2019).
[40] M. Yamada, M. Kondo, J. Mamiya, Y. Yu, M. Kinoshita, C. J. Barrett, and T. Ikeda, Photomobile polymer materials: Towards light-driven plastic motors, Angew. Chem. **47**, 4986 (2008).
[41] G. A. Bekey, *Autonomous Robots: From Biological Inspiration to Implementation and Control* (MIT Press, Cambridge, 2005).
[42] L. Zhou, Y. Dai, J. Fang, and K. Li, Light-powered self-oscillation in liquid crystal elastomer auxetic metamaterials with large volume change, Int. J. Mech. Sci. **254**, 108423 (2023).
[43] H. Wu, J. Lou, Y. Dai, B. Zhang, and K. Li, Bifurcation analysis in liquid crystal elastomer spring self-oscillators under linear light fields, Chaos Soliton Fract. **181**, 114587 (2024).
[44] H. Wu, J. Lou, B. Zhang, Y. Dai, and K. Li, Stability analysis of a liquid crystal elastomer self-oscillator under a linear temperature field, Appl. Math. Mech. (Engl. Ed.) **45**, 337 (2024).
[45] D. Ge, Y. Dai, and K. Li, Light-powered self-spinning of a button spinner, Int. J. Mech. Sci. **238**, 107824 (2023).
[46] X. Su, K. Li, W. Hu, and P. Xu, Self-sustained rolling of a liquid crystal elastomer rod under inclined light illumination, Int. J. Mech. Sci. **226**, 107411 (2022).
[47] Y. Hu, Q. Ji, M. Huang, L. Chang, C. Zhang, G. Wu, B. Zi, N. Bao, W. Chen, Y. Wu, Light-driven self-oscillating actuators with pototactic locomotion based on black phosphorus heterostructure, Angew Chem. Int. Edl. **60**, 20511 (2021).
[48] J. Sun, W. Hu, L. Zhang, R. Lan, H. Yang, D.-K. Yang, Light-driven self-oscillating behavior of liquid-crystalline networks triggered by dynamic isomerization of molecular motors, Adv. Funct. Mater. **31**, 2103311 (2021).
[49] Y. Kim, J. Berg, and A. J. Crosby, Autonomous snapping and jumping polymer gels, Nat. Mater. **20**, 1695 (2021).
[50] P. Xu, Y. Chen, H. Wu, Y. Dai, and K. Li, Chaotic motion behaviors of liquid crystal elastomer pendulum under periodic illumination, Results Phys. **56**, 107332 (2024).
[51] H. Wu, B. Zhang, and K. Li, Synchronous behaviors of three coupled liquid crystal elastomer-based spring oscillators under linear temperature fields, Phys. Rev. E **109**, 024701 (2024).
[52] Q. Cheng, W. Cheng, Y. Dai, and K. Li, Self-oscillating floating of a spherical liquid crystal elastomer balloon under steady illumination, Int. J. Mech. Sci. **241**, 107985 (2023).
[53] A. H. Gelebart, D. J. Mulder, M. Varga, A. Konya, G. Vantomme, E. W. Meijer, R. L. B. Selinger, and D. J. Broer, Making waves in a photoactive polymer film, Nature (London) **546**, 632 (2017).
[54] A. Chakrabarti, G. P. T. Choi, and L. Mahadevan, Self-excited motions of volatile drops on swellable sheets, Phys. Rev. Lett. **124**, 258002 (2020).
[55] A. W. Hauser, S. Sundaram, and R. C. Hayward, Photothermocapillary oscillators, Phys. Rev. Lett. **121**, 158001 (2018).
[56] M. P. da Cunha, A. R. Peeketi, A. Ramgopal, R. K. Annabattula, and A. P. H. J. Schenning, Light-driven continual oscillatory rocking of a polymer film, Chem. Open **9**, 1149 (2020).
[57] K. M. Herbert, H. E. Fowler, J. M. McCracken, K. R. Schlafmann, J. A. Koch, and T. J. White, Synthesis and alignment of liquid crystalline elastomers, Nat. Rev. Mater. **7**, 23 (2021).
[58] S. Residori, Patterns fronts and structures in a liquid-crystal-light-valve with optical feedback, Phys. Rep. **416**, 201 (2005).
[59] A. Piccardi, U. Bortolozzo, S. Residori, and G. Assanto, Spatial solitons in liquid-crystal light valves, Opt. Lett. **34**, 737 (2009).
[60] H. Xing, J. Li, J. Guo, and J. Wei, Bio-inspired thermal-responsive inverse opal films with dual structural colors based on liquid crystal elastomer, J. Mater. Chem. C **3**, 4424 (2015).
[61] H. Xing, J. Li, Y. Shi, J. Guo, and J. Wei, Thermally driven photonic actuator based on silica opal photonic crystal with liquid crystal elastomer, ACS Appl. Mater. Interfaces **8**, 9440 (2016).
[62] K. Li, Z. Chen, Z. Wang, and S. Cai, Self-sustained eversion or inversion of a thermally responsive torus, Phys. Rev. E **103**, 033004 (2021).
[63] Y. Wang, J. Sun, W. Liao, and Z. Yang, Liquid crystal elastomer twist fibers towards rotating microengines, Adv. Mater. **34**, 2107840 (2021).
[64] J. Liu, F. Shi, W. Song, Y. Dai, and K. Li, Modeling of self-oscillating flexible circuits based on liquid crystal elastomers, Int. J. Mech. Sci. **270**, 109099 (2024).
[65] Q. He, Z. Wang, Y. Wang, A. Minori, M. Tolley, and S. Cai, Electrically controlled liquid crystal elastomer–based soft tubular actuator with multimodal actuation, Sci. Adv. **5**, eaax5746 (2019).
[66] M. Li and P. Keller, Artificial muscles based on liquid crystal elastomers, Phil. Trans. R. Soc. A **364**, 2763 (2006).
[67] H. Wermter and H. Finkelmann, Liquid crystalline elastomers as artificial muscles, e-Polymers **1**, 013 (2001).
[68] D. Sun, J. Zhang, H. Li, Z. Shi, Q. Meng, S. Liu, and X. Liu, Toward application of liquid crystalline elastomer for smart robotics: State of the art and challenges, Polymers **13**, 1889 (2021).
[69] T. Zhao, Y. Zhang, Y. Fan, J. Wang, H. Jiang, and J. Lv, Light-modulated liquid crystal elastomer actuator with multimodal shape morphing and multifunction, J. Mater. Chem. C **10**, 3796 (2022).
[70] I. Steinberg, A. Oplatka, and A. Katchalsky, Mechanochemical engines, Nature (London) **210**, 568 (1966).
[71] M. Knežević and M. Warner, Optomechanical elastomeric engine, Phys. Rev. E **88**, 040501(R) (2013).

[72] M. Knežević and M. Warner, Optomechanical conversion by mechanical turbines, Phys. Rev. Appl. **2**, 044017 (2014).

[73] M. Saed and E. Terentjev, Siloxane crosslinks with dynamic bond exchange enable shape programming in liquid-crystalline elastomers, Sci. Rep. **10**, 6609 (2020).

[74] V. Domenici and B. Zalar, Paranematic-nematic phase transition in liquid crystalline elastomers: A ^{2}H-NMR study, Phase Transit **83**, 1014 (2010).

[75] M. Camacho-Lopez, H. Finkelmann, P. Palffy-Muhoray, and M. Shelley, Fast liquid-crystal elastomer swims into the dark, Nat. Mater. **3**, 307 (2004).

[76] P. Hogan, A. Tajbakhsh, and E. Terentjev, uv manipulation of order and macroscopic shape in nematic elastomers, Phys. Rev. E **65**, 041720 (2002).

[77] A. Baumann, A. Sánchez-Ferrer, L. Jacomine, P. Martinoty, V. Houerou, F. Ziebert, and I. Kulić, Motorizing fibers with geometric zero-energy modes, Nat. Mater. **17**, 523 (2018).